ISSN: 2414-1895 DOI: 10.6919/ICJE.202311_9(11).0012

Growth Process and Photoelectric Properties of $MoTe_2$/WTe_2 Heterojunction by CVD Method

Guanyi Bao

Jiangsu University, Zhenjiang, Jiangsu, China

Abstract

Transition metal chalcogenides (TMDs) are graphene-like materials. Molybdenum telluride ($MoTe_2$) is a unique material in TMDs, which can exist stably in 2H, Td and 1T 'phases. The possibility of implementing new topological states in materials other than insulators, such as semi-metals or metals, has attracted considerable attention. Weyl semi-metal (WSM) is a new state of matter in solid state physics. Molybdenum ($MoTe_2$) and tungsten (WTe_2) telluride are Weyl semi-metals and belong to the second class of Weyl semi-metals. The dirac cone near the Weyl point is inclined, so the corresponding electron dispersion relation near the Weyl point does not satisfy the symmetry of the Lorenz transform and has anisotropic negative reluctance. Its structure generates new physico-electrical properties, which in addition to being good topological and ferromagnetic materials, also has certain potential in the field of optoelectronics. $MoTe_2$ has good photocurrent response in scanning tunneling microscope (STM), which can be used as a new photodetector. In this paper, $MoTe_2$ and WTe_2 films with different regular morphologies were grown under different conditions by CVD synthesis method, and heterojunction was synthesized. The film was characterized by different tests, and the electrode was plated on the surface of the film by thermal evaporation method to explore its photoelectric characteristics.

Keywords

Chemical Vapor Deposition; Molybdenum Telluride; Tungsten Telluride; Heterojunction control.

1. Introduction

Transition metal dihalides (TMDs) have attracted great interest over the past two decades due to their interesting physical properties and broad application prospects, and of all the TMDs, the metal tellurides (MTe_2, M stands for a transition metal atom) has a much longer carrier lifetime and band gap than the corresponding metal sulfides (MS_2) and selenides (MSe_2), therefore, tellurides with various nanostructures are considered to be excellent candidates for the study of fundamental physical phenomena such as superconductivity and thermoelectric conversion, photoelectric effect, etc[1,2].

Both $MoTe_2$ and WTe_2 are Weyl semi-metals of the second kind. The Weyl semi-metal is a novel quantum state in which the electron dispersion relationship exists in pairs of chiral opposite Weyl points. The Weyl points can be regarded as a pair of positive and negative magnetic charges in inverted space near this point. Electrons in the material as quasi particles have the same motion characteristics as massless Weyl fermions[3].

In this paper, the morphologies of the grown films were observed and recorded by metallographic optical microscopy, atomic force microscopy and scanning electron microscopy, and characterized by Raman, XRD and EDS.

ISSN: 2414-1895 DOI: 10.6919/ICJE.202311_9(11).0012

The synthesized $MoTe_2$ has two different morphologies. In the hydrogen-containing environment, the film morphology is mostly 3-5μm sheet morphology, while in the non-hydrogen-containing environment, the film morphology is mostly 10-30μm nanowires with changing air pressure and flow state. The calculated band gap Eg=1.60eV of $MoTe_2$ nanowires indicates that it is a potential visible light active material[4,5]. WTe_2 is an important layered transition metal dihalogenated hydrocarbon compound[6]. In this paper, the square shape of WTe_2 thin films with the size of 3~7μm has been grown by CVD method, which will provide guidance for large-scale synthesis of WTe_2 in the future. The van der Waals heterojunction of WTe_2-$MoTe_2$ nanowires was prepared successfully, and the photoelectric properties of the heterojunction were investigated in this research.

2. Experimental

The smooth surface SiO_2 was selected as the substrate and placed in propyl ethanol for ultrasonic cleaning. Materials were synthesized by two-step method and one-step method respectively. Firstly, $MoTe_2$ was synthesized on the substrate by double-zone furnace method, and then WTe_2 was synthesized on this basis[7]. 0.4g tellurium powder and 0.2g MoO_3 powder (mixed and ground with 0.1gNacl) were placed into a quartz boat. The boat was then placed in the center of a heating zone and heated to 690℃ and 720℃ for 37min under vacuum in a heating furnace. Heat preservation in Ar/H_2 flowing gas for 40min (Ar=25sccm, H_2=15sccm). After telluride treatment, the powder was cooled to room temperature, then 0.4g tellurium powder and 0.25gWO_3 powder (mixed with 0.1gNacl for grinding) were put into a quartz boat and heated to 690℃ and 790℃ respectively for 37min. The powder was kept in Ar/H2 flowing gas for 40min (Ar=25sccm, H2=15sccm), and finally cool down to room temperature.

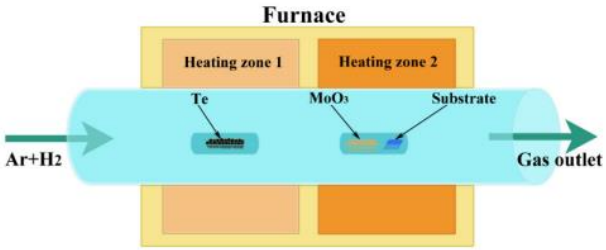

Fig. 1 Flow chart of MoTe2 synthesis in double temperature zone.

Secondly, 0.2gMoO_3, 0.25gWO_3 and 0.2gNacl powder mixture were ball mused for 12h by a ball mill, and 0.8g tellurium powder and 0.8g tellurium powder were respectively put into a quartz boat and heated by two-zone furnace method. After vacuuming, the heating furnace was heated to 690℃ and 790℃ respectively for 37min. The heating time was 40min in Ar/H_2 flowing gas (Ar=25sccm, H2=15sccm), and finally cooled down to room temperature.

3. Results and Conclution

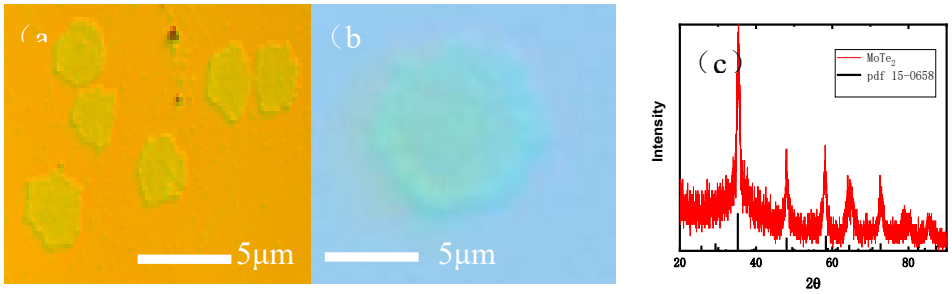

Fig. 2 (a),(b) Lamellar $MoTe_2$ under optical microscope; (c) XRD pattern of $MoTe_2$.

ISSN: 2414-1895 DOI: 10.6919/ICJE.202311_9(11).0012

The synthesized $MoTe_2$ has the following two structures, one is regular hexagon, the other is nanowire microstructure.

Fig.2 (a), (b) shows the optical microscope morphology of $MoTe_2$ synthesized by low pressure CVD method in hydrogen environment, with clear boundary and size of about 3-6 μm. (c) shows the XRD pattern of $Mote_2$ (JCPDS Card 15--0658). It is proved that the prepared hexagonal film is molybdenum ditelluride ($MoTe_2$).

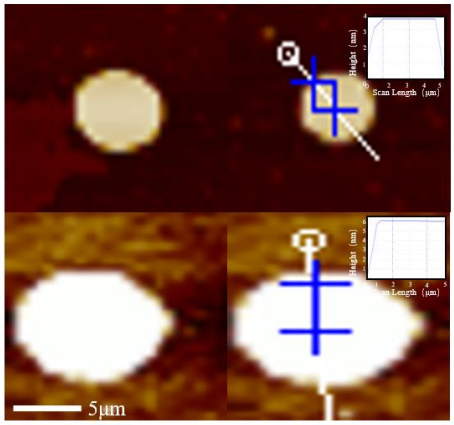

Fig. 3 $MoTe_2$ AFM topography.

Fig.3 shows the AFM topography of $MoTe_2$. The surface is smooth and flat, and the thickness is about 4-6 μm.

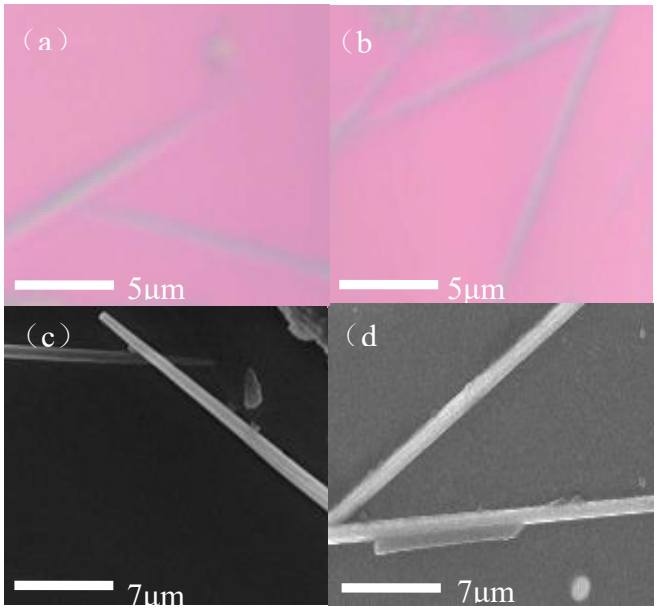

Fig.4 (a),(b) Optical microscope image of $MoTe_2$ nanowire;(c),(d) SEM image of nanowires.

Fig.4 shows that in the absence of hydrogen gas, $MoTe_2$ synthesized by CVD method showed a nanolinear structure. By optical microscopy (FIG. 4 (a) and (b)) and scanning electron microscopy (SEM)(FIG. 4 (c) and (d)), the prepared MoTe2 nanowires were observed to have complete structures and varying lengths. Its diameter is about 5~6nm and its length is about 10~20μm. It can be seen by SEM that the film thickness of the product is relatively uniform and the surface is relatively smooth.

ISSN: 2414-1895 DOI: 10.6919/ICJE.202311_9(11).0012

Because the tilt Angle of the quartz boat where the Mo source and the substrate are located is increased, the grown film has obvious stratification and vein, and the same growth direction can better obtain the lamellar film. However, due to the instability of the air flow, some cracks will appear in the structure of the product, and further improvement of the experimental conditions may be able to obtain a smooth single-layer film growing in a larger area.

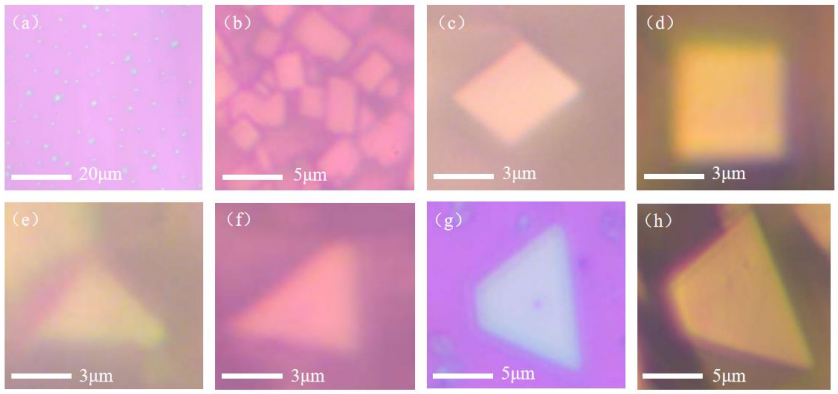

Fig.5 optical microscope images with different morphologies of WTe_2

Fig.5 (a~f) shows the 2D lamellae WTe_2 optical microscope images with different morphologies prepared by us, which can indicate that relatively uniform samples are prepared, with the size of a single film about 3~5μm. When the growth temperature zone of W source is set to 720°C, the aggregation degree of the films with a growth time of 20min and 60min is greatly different, as shown in Fig.5 (a) and (b). In fig.5 (a), when the growth time is 20min, most of the films are discrete and have irregular morphology, and some of them are regular triangles or trapezoids, as shown in Fig.5 (e~h). This is because the growth time is not enough, which makes the reaction between Te and WO_3, including the reaction between WO_3 and $NaCl$, insufficient, and eventually some impurities will be deposited on the substrate, forming irregular morphology. However, after the nucleation of WTe_2 deposited on the substrate, the growth trend toward the four corners is inconsistent, and WTe_2 will preferentially extend and grow rapidly toward one of the two corners, reach the boundary saturation, and then make up for the other two corners, and finally achieve complete saturation of the stress equilibrium boundary, forming a regular rectangular morphology of laminates, as shown in Fig.5 (c) and (d), with clear boundaries and smooth surfaces. In addition, a single WTe_2 film has certain exclusivity after reaching the boundary saturation state, and will not destroy its own boundary saturation state even if dense aggregation, and multiple films are stacked in a stacked manner[8], as shown in Figure (b).

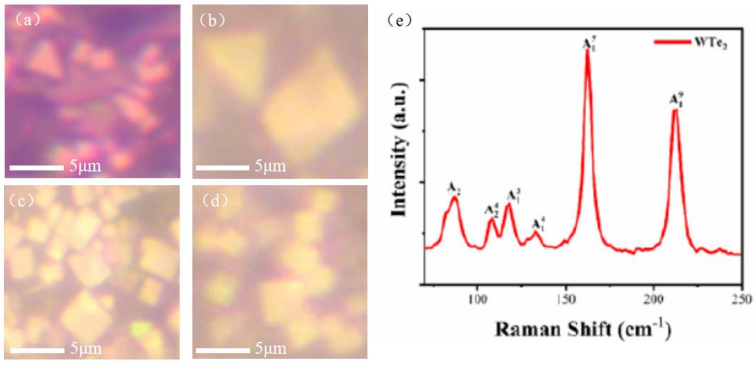

Fig.6 (a),(b),(c) are WTe_2 under different growth duration;
(d)Dense packing 1T'-WTe_2;(e)Raman of 1T'-WTe_2

ISSN: 2414-1895 DOI: 10.6919/ICJE.202311_9(11).0012

In order to verify the angular tendency of the growth mechanism of WTe_2, we observed the films with a growth time of 30min, 40min and 50min respectively, as shown in Fig.6 (a~c). It can be found that as the growth time increases, irregular morphology disappears, triangular and trapezoidal morphology gradually decreases, while regular rectangular morphology increases. When the growth time is 50min, most of the films grow completely, in a regular rectangular shape, and will be densely stacked. Fig.6 (d) clearly highlights the boundary saturation of WTe_2 films when they are densely packed. When the growth reaches saturation, it will not continue to extend and grow, and other nearby nucleated WTe_2 will squeeze and limit its growth. Fig.6 (e) shows its Raman scattering spectra, with characteristic peaks at 87.3cm-1, 161.1cm-1 and 210.6cm-1, proving that the thin film with regular rectangular morphology is 1T '-WTe_2.

We selected 1T '-WTe_2 thin films with regular rectangular morphology for SEM analysis, as shown in Fig.7, where (a), (b) are discrete distribution, and (c) are stacked distribution. It can be seen that the boundary of 1T '-WTe_2 film is clear, the surface is smooth and flat, and the size is about 3~5μm, indicating that the film has the properties of angular tendency and boundary saturation during the growth process.

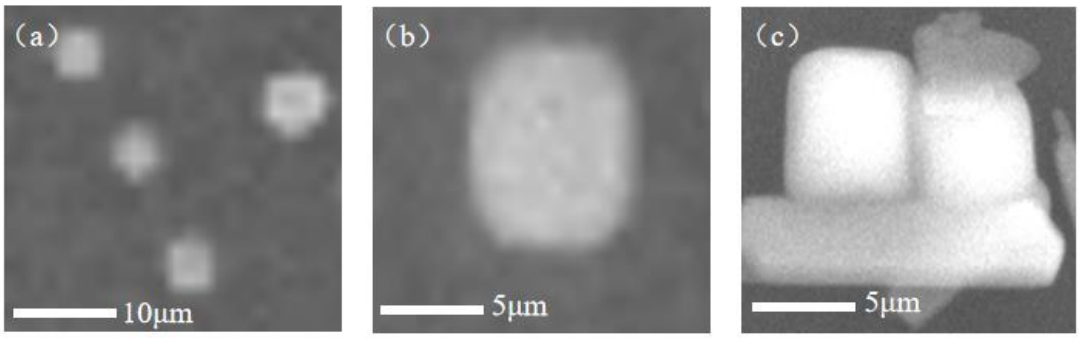

Fig.7 SEM of 1T'-WTe_2

According to theoretical and computational analysis, it can be seen that the three common crystal phase structures in TMDCs materials are 1T, 2H and 3R phases[9], representing the octahedral coordination tetragonal crystal system, hexagonal symmetric crystal system and rhombosymmetric crystal system respectively. In addition, there are also some transition phases, such as 2Hd and Td[10], which change due to different stacking modes between atomic layers. In this paper, 1T '-WTe_2 synthesized by CVD method belongs to tetragonal crystal system and can exist stably. The morphology and crystal structure of 1T'-WTe_2 are analyzed as follows.

There is a certain relationship between crystal morphology and crystal structure, but it is difficult for us to directly judge the final crystal shape through crystal system, space group and chemical composition, and the final crystal shape is closely related to the growth environment (temperature, pressure, solvent and solute concentration, etc.) and other influencing factors. The cell is the smallest repeating unit that can reflect the symmetry of the crystal, so a large single crystal itself can be understood as being obtained by the translation operation of the cell. The morphology of a single crystal depends on the shape constructed on the surface of the final crystal exposed[11]. For a large enough crystal, no matter what kind of crystal system it belongs to, as long as the specific exposure surface is selected, most of the required shapes can be constructed, of course, for some special shapes, the required exposure surface is more, and even cannot be constructed at this stage (such as the ideal spherical crystal)[12].

However, if only the natural growth process of the crystal is considered, then the crystal structure is bound to have an impact on the crystal shape, in Wulff construction, its theoretical basis is Gibbs-Wulff crystal growth law: Under the condition of isothermal constant volume, if the total surface energy of the crystal is minimum, the corresponding state is the equilibrium state of the crystal. The

ISSN: 2414-1895 DOI: 10.6919/ICJE.202311_9(11).0012

linear growth rate of a family of crystal faces is proportional to the specific surface free energy of the family of crystal faces[13] :

$$\frac{\sigma_1}{r_1} = \frac{\sigma_2}{r_2} = \cdots = \frac{\sigma_i}{r_i}$$

Where σi is the specific surface free energy of i-th the crystal face, and ri is the distance from the center of the crystal with an equilibrium form to the i-th crystal face. In short, for the growth of atoms at the nanoscale, the lower the surface energy, the faster the growth rate of the crystal face. Therefore, when crystal growth is a thermodynamically controlled growth process, the shape chosen by a crystal during growth will be one that minimizes the surface free energy, Gibbs once proposed that the Gibbs free energy of the crystal surface can be written as[14]:

$$\Delta G_i = \sum_j \gamma_j O_j$$

Where γj represents the surface energy per unit area of the j-th crystal face. The surface energy of a specific crystal face depends on many factors, such as the chemical properties of the crystal face itself, including chemical composition, atomic coordination structure and coordination number[15]. In the real environment, the crystal is bound to interact with some substances, such as impurities on the surface of adsorbed substances, which will have an impact on the crystal surface, and during the growth process of the crystal, the concentration of the precursor will change at any time, which will affect the final morphology of the crystal.

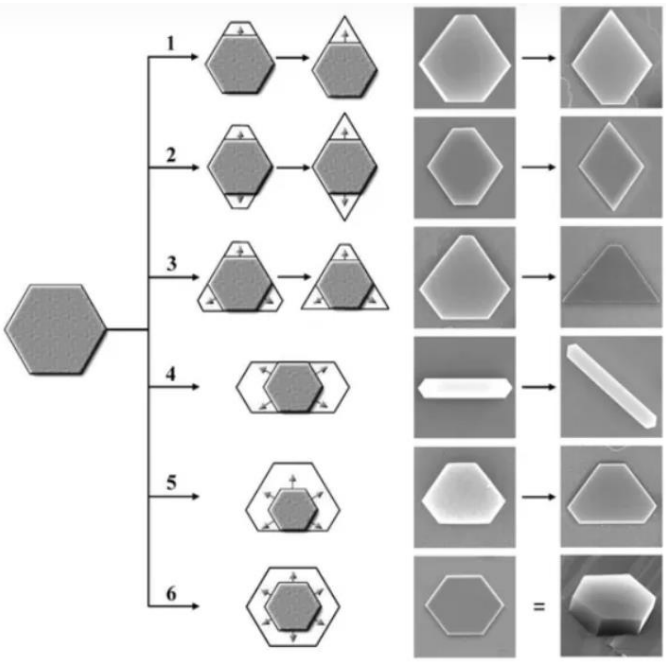

Fig.8 Crystal growth trend in Wulff construction[16]

In the vacuum environment, the carrier gas flow is kept stable, the heating rate is adjusted, the concentration of precursor in the cavity is increased, so that Te and WO_3 can fully react. At the same time, the Angle between the quartz boat and the plane where the substrate is located is regulated, so that the film can expand and grow better after the nucleation of WTe_2, and the influence of stress

ISSN: 2414-1895 DOI: 10.6919/ICJE.202311_9(11).0012

extrusion on its angular tendency can be reduced. Thus, a rectangular 1T'-WTe_2 with relatively complete morphology was obtained. According to the morphology study of crystal growth of Wulff construction, there are different growth trends[16] as shown in Fig.8, which well explains the different morphologies of the same crystal in the plane layer. In the case of insufficient growth time, the angular tendency of 1T'-WTe_2 is relatively obvious, and more WTe_2 crystals tend to preferentially grow toward two angles, forming triangular and trapezoidal morphology, as shown in step 3 of Fig.8. However, when the reaction is relatively sufficient and the film growth time is sufficient, the WTe_2 crystal can extend and grow evenly toward the four corners, as shown in Fig.8 Step 4, so as to obtain more regular rectangular morphology. Besides stress, other factors affect the boundary saturation of WTe_2 film growth.

Without changing other experimental conditions, we continued to explore the growth mechanism of 1T'-WTe_2 by replacing different substrates, and found that 1T'-WTe_2 films growing on smooth surfaces and rough surfaces would be slightly different, as shown in Fig. 9 below. In the previous section, we obtained that the 1T'-WTe_2 film grown on a smooth surface would have two cases of discrete distribution and dense packing. In addition to discrete distribution, the thin film grown on the rough surface will also have a large area of planar extension growth, as shown in Fig.9 (a). It can be seen that the surface of WTe_2 growing on a rough surface is not smooth, and the van der Waals forces between atomic layers are unevenly applied, as shown in Fig.9 (b), (c), and its nucleation points and obvious boundaries can be seen. According to the Gibbs-Wulff law of crystal growth[17], the specific surface free energy of a WTe_2 crystal grown on a rough surface is much larger than that of a WTe_2 crystal grown on a smooth surface, so that subsequent crystals will not be induced to grow vertically on its surface. The 1T'-WTe_2, which grows on both rough and smooth surfaces, has two properties: angular tendency growth and boundary saturation. At the same time, we can obviously observe that there is a repulsion between the short distance nucleation points of the film grown on the rough surface. Due to the effect of stress extrusion, a single WTe_2 crystal film cannot grow completely, which limits the angular tendency of most WTe_2 growth, and its boundary cannot reach full saturation. Due to the different nucleation time, growth rate and Angle inclination direction, the grown films are mostly irregular polygon morphologies.

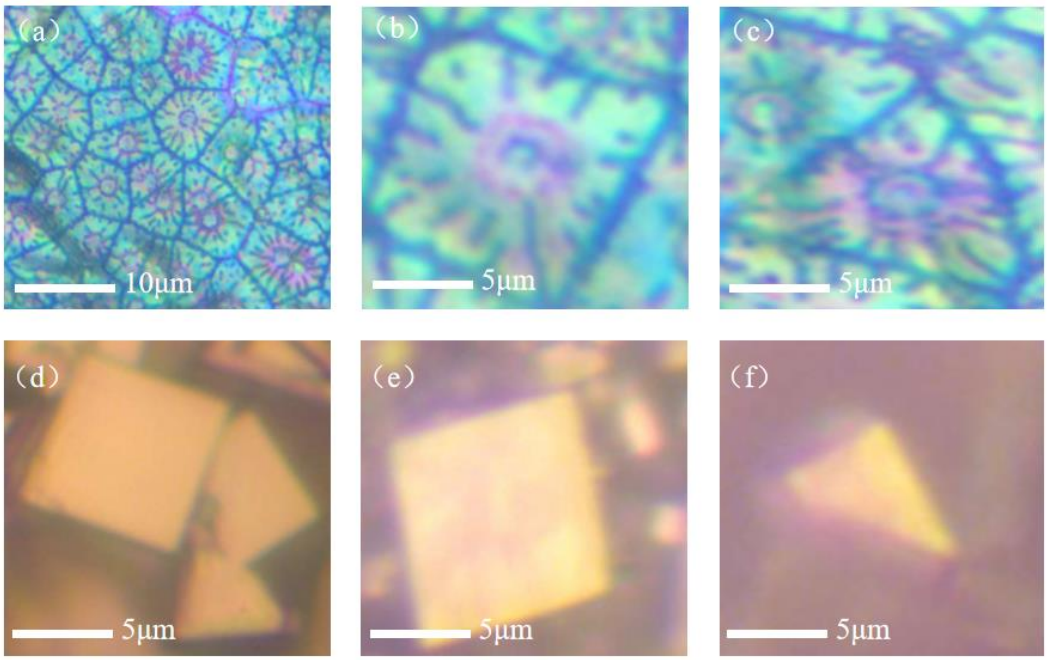

Fig.9 Morphology of 1T '-WTe_2 grown on different substrates

ISSN: 2414-1895 DOI: 10.6919/ICJE.202311_9(11).0012

Fig.10 shows the WTe_2 AFM spectrum of different surface growth. It can be seen that the surface of the film grown on the rough surface in (a) and (b) is not smooth and flat, while the surface of the film grown on the smooth surface in (c) and (d) is relatively smooth and flat. The prepared WTe_2 films all have obvious boundaries, and the thickness is about 3~5nm. This reflects from the side that the WTe_2 film has the properties of angular tilt and boundary saturation during growth. Under the environment of smooth surface, suitable precursor volume, stable growth temperature (720°C) and suitable growth time (50~60min), the 1T'-WTe_2 film with regular rectangular morphology can be obtained well.

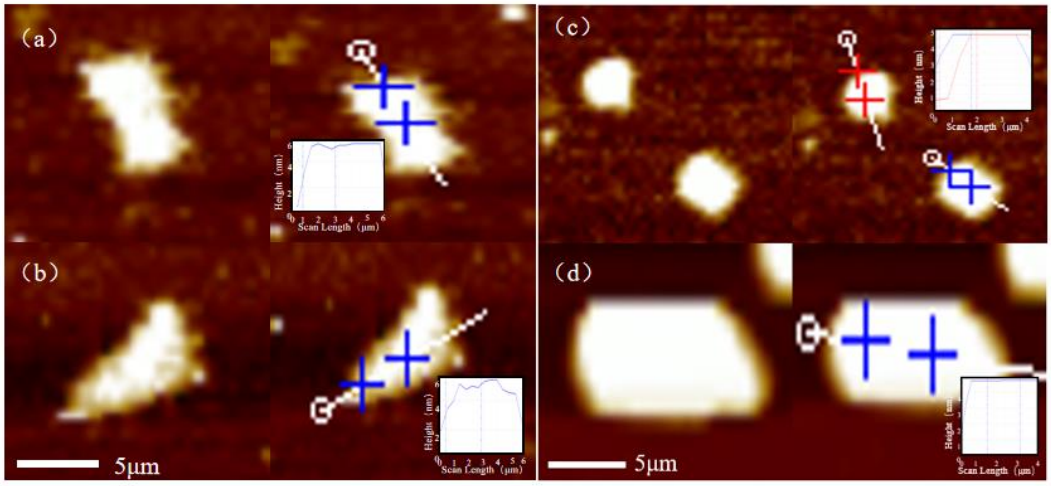

Fig. 10 AFM of different morphologies of WTe_2

In Fig.11 (a) and (b) for the optical microscope map of heterojunction growth on smooth surfaces. The obtained $MoTe_2$ and WTe_2 films are both 1T' phase, and their surfaces are smooth and flat with obvious boundaries. (c), (d) represent the SEM morphology of the heterostructures, and the contact positions formed by the heterostructures can be seen. The grown $MoTe_2/WTe_2$ heterostructures form a vertical spliced structure.

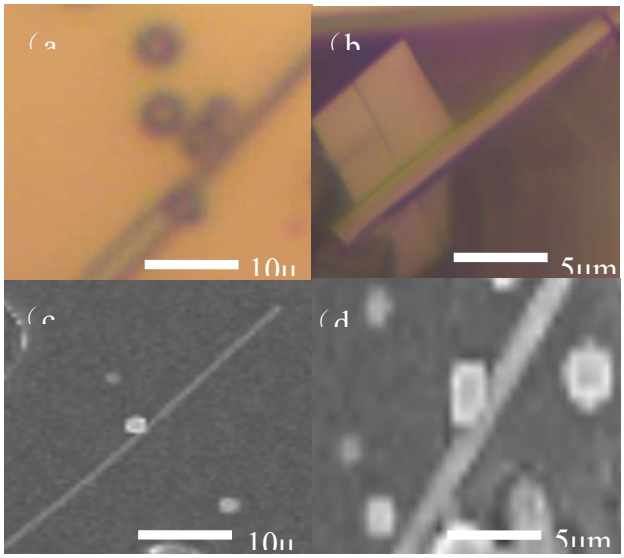

Fig.11 (a),(b) optical microscope morphology of $MoTe_2/WTe_2$ heterojunction; (c) and (d) are SEM morphology

By constructing electrodes on the heterojunction with a self-built platform, it is found that the photoluminescence effect can be produced under near-infrared light (λ=800nm) irradiation. Fig.12 (a)

ISSN: 2414-1895 DOI: 10.6919/ICJE.202311_9(11).0012

shows the EDS pattern of $MoTe_2/WTe_2$ heterojunction,which verifies that the grown heterojunction is $MoTe_2/WTe_2$ heterojunction. (b) is the total spectrum of atomic proportion, in which Te atoms account for 65.6%, Mo atoms account for 16.8%, and W atoms account for 17.6%. (c) is the XRD characterization pattern of $MoTe_2/WTe_2$ heterojunctions, which can distinguish the characteristic peaks of $MoTe_2$ and WTe_2, and partial migration will occur, which is caused by the strong coupling interaction between the heterojunctions. Fig.12 (d) shows that $MoTe_2/WTe_2$ heterojunction can generate photocurrent at 4V voltage. Due to the small contact area of the heterojunction grown by CVD, its photoelectric effect is not as obvious as that of mechanical stripping method. (e) for its time-response map, it is determined that $MoTe_2/WTe_2$ heterojunction can produce photogenic volt effect under near-infrared light (λ=800nm) irradiation. Under the irradiation of near infrared light, atoms in $MoTe_2/WTe_2$ heterojunction are excited by photon absorption. When photon energy is greater than band gap, non-equilibrium carriers of electron-hole pair will be generated. Under the action of the built-in electric field, holes move to the P region and electrons move to the N region, forming a photogenerated electric field in the opposite direction of the built-in electric field. Therefore, the photoelectromotive force is established in the P region and N region.

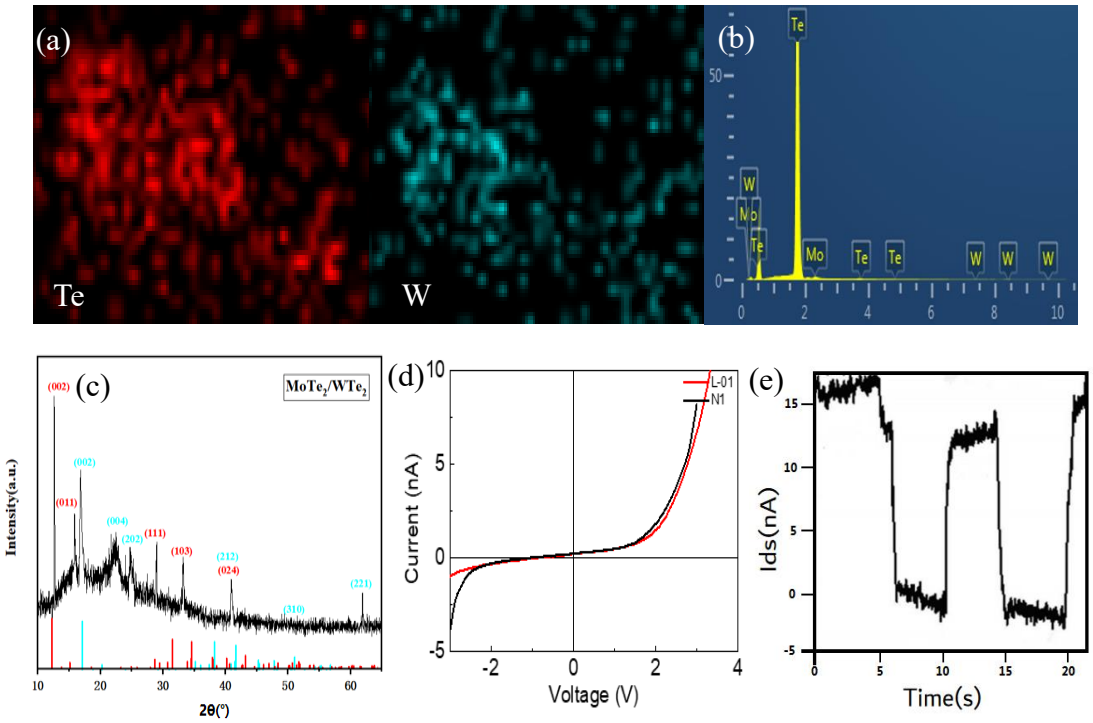

Fig.12 (a),(b) EDS map of $MoTe_2/WTe_2$ heterojunction;(c) XRD pattern of $MoTe_2/WTe_2$ heterojunction; (d) Photocurrent generated by $MoTe_2/WTe_2$ heterojunction at 4V voltage; (e) Time response map

4. Discussion

Semiconductor materials absorb photons in incident light radiation, resulting in additional free electrons and free holes in the material, thereby changing the conductivity of the semiconductor. Fig.13 (a) shows the structural band diagram of $MoTe_2/WTe_2$ heterojunction under light conditions. The electron affinity of $WTe_2(MoTe_2)$ is 4.4eV(3.8eV), and the band gap of a few layers of $MoTe_2$ is 1.0eV[17]. The difference makes it possible to separate the photogenerated electron-hole in the heterojunction.

When the external optical power P is incident, a photocurrent is generated inside the semiconductor[18]:

ISSN: 2414-1895 DOI: 10.6919/ICJE.202311_9(11).0012

$$i_p = \frac{\alpha P \tau_0 \mu e}{h\gamma L} \int_0^d exp(-\alpha x) dx$$

When all the incident light energy is absorbed by the corresponding photodetector, the average photo-generated carrier concentration is[18]:

$$n_0 = \frac{P\tau_0}{WLdh\gamma}$$

In this case, the corresponding photocurrent generated is $i_{p0} = \frac{P\tau_0 \mu e}{h\gamma L}$, Quantum efficiency is $\eta = \frac{i_p}{i_{p0}} = \alpha \int_0^d exp(-\alpha x) dx$, Then the photocurrent can be expressed as:

$$i_p = \frac{\eta P e}{h\gamma}\left(\frac{\tau_0 \mu}{L}\right) = \frac{\eta P e}{h\gamma} \cdot \frac{\tau_0}{\tau_d} = G \cdot \frac{\eta e}{h\gamma} \cdot P$$

Where τd is the time for the photogenerated carrier to cross between electrodes, G is the internal gain of the photodetector, and Fig.13 (b) is the calculated value of the photoconductivity of the single-layer thin film. The calculated spectrum is obtained when the Fermi level is 0eV, and the component of the interband conductivity involves the transition between occupied and unoccupied states. The Weyl point of $MoTe_2$ and WTe_2 is usually located in the conduction region (55mev and above), where the calculated photoconductivity of single-layer $MoTe_2$ film is 1.37-1.95 eV, and the calculated photoconductivity of single-layer WTe_2 film is 0.34-0.49 eV[19]. Fig.13 (c) shows the schematic diagram of the photoelectric effect of $MoTe_2/WTe_2$ heterojunction. According to theoretical calculations, the Fermi levels of WTe_2 and $MoTe_2$ are fixed[20] and can be modulated in the entire band gap through the external gate voltage respectively. In order to detect the characteristics of the transition involving the band forming the Weyl point, the Fermi level must be raised accordingly without affecting the rest of the electronic structure.

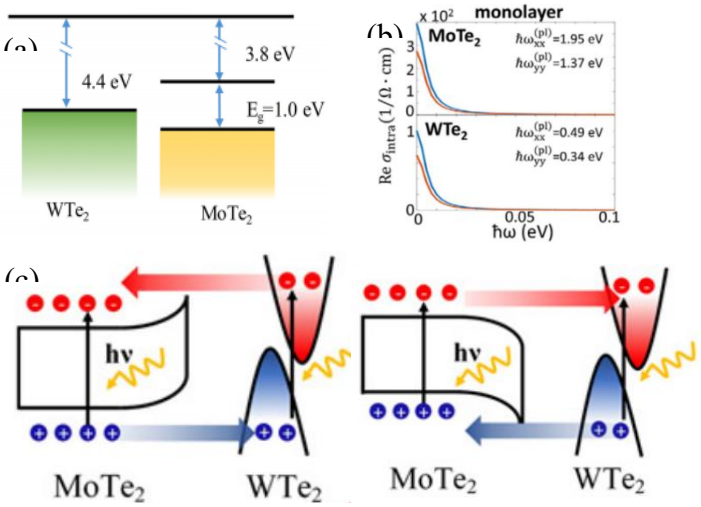

Fig.13 (a) Structural band map of $MoTe_2/WTe_2$ heterojunction under light condition;
(b) Calculation value of photoconductivity of single layer film;
(c) Schematic diagram of photoelectric effect in $MoTe_2/WTe_2$ heterojunction

ISSN: 2414-1895 DOI: 10.6919/ICJE.202311_9(11).0012

References

[1] T. Kim, D. Kang, Y. Lee, S. Hong, H.G. Shin, H. Bae, Y. Yi, K. Kim, S. Im, Adv. Funct.Mater. 30 (2020) 2004140.

[2] K. Chen, Z. Chen, X. Wan, Z. Zheng, F. Xie, W. Chen, X. Gui, H. Chen, W. Xie, J. Xu, Adv. Mater. 29 (2017) 1700704.

[3] W.G. Dawson, D.W. Bullett, J. Phys. C: Solid State Phys. 20 (1987) 6159–6174.

[4] M.K.Jana, A. Singh,D.J. Late,C.R. Rajamathi, K. Biswas, C. Felser, U.V. Waghmare, C.N.R. Rao, J. Phys.: Condens. Matter. 27 (2015) 285401.

[5] Y. Wei, C. Deng, X. Zheng, Y. Chen, X. Zhang, W. Luo, Y. Zhang, G. Peng, J. Liu, H. Huang, W. Cai, Q. Ge, R. Zhang, X. Zhang, S. Qin, Nano Res. 15 (2022) 401–407.

[6] K. Buchkov, R. Todorov, P. Terziyska, M. Gospodinov, V. Strijkova, D. Dimitrov, V. Marinova, Nanomaterials. 11 (2021) 2262.

[7] E. Wu, Y. Xie, J. Zhang, H. Zhang, X. Hu, J. Liu, C. Zhou, and D. Zhang, Sci.Adv. 5, eaav3430 (2019).

[8] Z. Zhang, Z. Wang, T. Shi, C. Bi, F. Rao, Y. Cai, Q. Liu, H. Wu, and P. Zhou, InfoMat 2, 261 (2020).

[9] C. Liu, H. Chen, S. Wang, Q. Liu, Y. G. Jiang, D. W. Zhang, M. Liu, and P. Zhou, Nat. Nanotechnol. 15, 545 (2020).

[10] C. Y. Wang, S. J. Liang, S. Wang, P. Wang, L. Zhu'an, Z. Wang, A. Gao, C. Pan, C. Liu, J. Liu, H. Yang, X. Liu, W. Song, C. Wang, B. Cheng, X. Wang, K. Chen, Z. Wang, K. Watanabe, T. Taniguchi, J. J. Yang, and F. Miao, Sci. Adv. 6, eaba6173 (2020).

[11] K. Zhang, T. Zhang, G. Cheng, T. Li, S. Wang, W. Wei, X. Zhou, W. Yu, Y. Sun, P. Wang, D. Zhang, C. Zeng, X. Wang, W. Hu, H.J. Fan, G. Shen, X. Chen, X. Duan, K. Chang, N. Dai, ACS Nano. 10 (2016) 3852–3858.

[12] Y. Xie, E. Wu, G. Geng, D. Zhang, X. Hu, J. Liu, Appl. Phys. Lett. 118 (2021).

[13] E. Torun, H. Sahin, S. Cahangirov, A. Rubio, and F. M. Peeters, J. Appl. Phys. 119, 074307 (2016).

[14] Y. Liu, P. Stradins, and S. H. Wei, Sci. Adv. 2, e1600069 (2016).

[15] I. G. Lezama, A. Arora, A. Ubaldini, C. Barreteau, E. Giannini, M. Potemski, and A. F. Morpurgo, Nano Lett. 15, 2336 (2015).

[16] A. Popescu, A. Pertsova, A.V. Balatsky, L.M. Woods, Adv. Theory Simul. 3 (2020) 1900247.

[17] Z. Zhu, X. Lin, J. Liu, B. Fauqué, Q. Tao, C. Yang, Y. Shi, K. Behnia, Phys. Rev. Lett. 2015, 114, 176601.

[18] C. C. Homes, M. N. Ali, R. J. Cava, Phys. Rev. B 2015, 92, 161109.

[19] H. Li, D. Li, H. Luo, Phys. Status Solidi B. 257 (2020) 2000006.

[20] Hasan M Z and Kane C L. Colloquium: Topological insulators [J]. Reviews of Modern Physics, 2010, 82(4): p. 3045-3067.